

Characteristics of a radio-frequency micro-dielectric barrier discharge array

Jun-Chieh Wang¹, Napoleon Leoni², Henryk Birecki², Omer Gila² and Mark J Kushner^{1,3}

¹ Department of Electrical Engineering and Computer Science, University of Michigan, Ann Arbor, MI 48109, USA

² Hewlett Packard Research Labs, Palo Alto, CA 94304, USA

E-mail: junchwan@umich.edu, napoleon.j.leoni@hp.com, henryk.birecki@hp.com, omer.gila@hp.com and mjkush@umich.edu

Received 20 January 2013, in final form 28 February 2013

Published 28 March 2013

Online at stacks.iop.org/PSST/22/025015

Abstract

Micro-dielectric barrier discharges (mDBDs) are known for being stable, high-pressure and non-thermal plasma sources. mDBD arrays consist of micro-plasma devices (10–100 μm) in which the radio frequency (rf)-excited electrodes are covered by dielectrics. In certain applications, independent control of individual mDBDs in an array is required for charge extraction to treat dielectric surfaces. When using the mDBDs to produce plumes of charged species, there are potential direct or indirect interactions between the mDBD devices. In this paper, we discuss the characteristics of atmospheric mDBD arrays sustained in N_2 with an O_2 impurity using results from a two-dimensional simulation. The device of interest consists of a sandwich structure using layers of dc and rf biased electrodes to help shape the plume. We found that the adjacency of the mDBDs and the dielectric properties of the materials being treated are important to the interactions between mDBDs in the array. Scaling laws are presented for operating characteristics of these mDBD arrays as a function of material properties, geometry, driving voltage waveform and gas mixture.

(Some figures may appear in colour only in the online journal)

1. Introduction

Dielectric barrier discharges (DBDs) are typically stable, high-pressure and non-thermal plasma sources in which the discharge is sustained between parallel electrodes covered by dielectrics [1]. The electrodes are driven with alternating voltages at frequencies as high as radio frequency (rf). DBDs are often used for atmospheric-pressure plasma generation due to their nearly arc-free operation, and so have found a wide range of applications, such as remediation of toxic gases and ozone generation [2, 3], ultraviolet/vacuum ultraviolet (UV/VUV) photon sources and surface modification [4–7], and medical applications [8, 9]. Arrays of micro-DBDs (or mDBDs) having dimensions of tens of micrometers operating at atmospheric pressure using rf voltages have been developed for large-area selective surface treatment and production of photons, excited states or charge species [10, 11]. mDBD

characteristics are determined by the geometry of the aperture, material, repetition rate and pulse shape, the latter two of which can, in principle, be independently controlled for each aperture [7, 10–17]. One such example of independent control of light-emitting mDBDs is the commercial plasma display panel (PDP).

mDBD arrays also hold potential for inexpensive latent image production in electrographic printing. Leoni *et al* developed an electrographic apparatus consisting of arrays of individually addressable mDBDs from which plumes of electron current, only tens of micrometers in diameter, are extracted for forming a latent image [18]. The mDBD is typically operated in nitrogen or in an inert gas to avoid the production of negative ions, which reduces the current extraction. These electron beams deposit a charge on the dielectric imaging surface. The charge is then either directly the basis of adhering toner particles to the surface or is transferred to another surface. During the formation of

³ Author to whom any correspondence should be addressed.

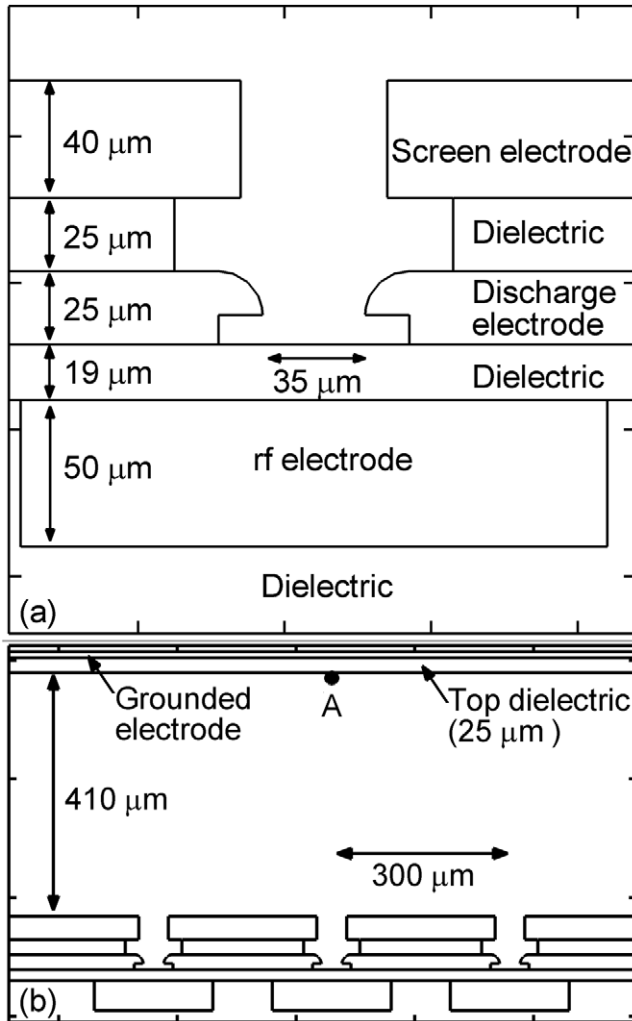


Figure 1. Schematic of the mDBD device. (a) A single mDBD aperture. (b) Multiple mDBD apertures and the top grounded electrode covered with a dielectric.

the latent image, the negative charge previously deposited on the imaging surface can repel the incoming electron current, thereby spreading and increasing the diameter of the initially narrow electron beam extracted from the mDBD. This divergence reduces the quality of the latent image [18, 19].

In addition to the interaction between mDBDs through dielectric charging, plumes of charge extracted from the mDBD apertures can also directly interact with each other or with the remnants of charge from previous discharge pulses. Although not a topic of this paper, combinations of indirect interactions with charged surfaces and direct interaction between DBD plumes, either attraction or repulsion, can result in self-organized patterns [20–25].

In this paper, we discuss results from a numerical investigation of a three-aperture array of mDBDs sustained in atmospheric-pressure N_2 with an O_2 impurity. The model geometry of the mDBD aperture, shown in figure 1, is patterned after those developed for electrographic printing [18]. We found that the divergence of the extracted current can be delayed by increasing the permittivity of the target surface to produce a longer charging time. Accumulation of positive

charge in the gap on a pulse-to-pulse basis helps one to extract electrons from the mDBD cavity. With higher oxygen impurity content, electron attachment begins to dominate, which reduces the extraction field and ultimately reduces the collected surface charge density. At rf frequencies up to 25 MHz, charge extraction is limited by the duration of the cathodic portion of the cycle. At lower frequencies having periods longer than the charging time of the intervening dielectric, the electron current is limited by charging of the dielectric. The model used in this investigation is described in section 2 and is followed by a discussion of N_2 plasma dynamics sustained in a single mDBD in section 3. In section 4, characteristics of the mDBD arrays are discussed, and section 5 contains our concluding remarks.

2. Description of the model

In this study, a two-dimensional (2D), fluid hydrodynamic simulation platform, *nonPDPSIM*, was used and is described elsewhere [26, 27] in detail. Briefly, *nonPDPSIM* simultaneously solves continuity equations, the surface charge balance equation and Poisson's equation for all charged species densities and electric potential. The electron energy equation is solved for the bulk electron temperature. The rate coefficients and transport coefficients for bulk electron transport are obtained by solving Boltzmann's equation for the electron energy distribution function (EEDF). The generation of UV/VUV radiation produced by relaxation of high-lying excited states of N_2 , and its transport, is addressed using a Green's function approach. An electron Monte Carlo simulation is used to track the ionization and excitation produced by sheath-accelerated secondary electrons. The source of secondary electrons includes ion and photon fluxes onto surfaces. The secondary emission coefficients used in this investigation were 0.15 and 0.1 for all positive ions and photons. Electrons are emitted with a Lambertian (cosine) distribution perpendicular to the local surface with an energy of 3 eV.

The mDBD is a sandwich of alternating electrodes and dielectrics (see figure 1). An rf biased metal electrode is embedded in a dielectric substrate (relative permittivity $\epsilon_r = \epsilon/\epsilon_0 = 4.3$) 50 μm below the dielectric surface. This rf electrode is biased with a -2 kV dc and a 1.4 kV ac potential with frequencies up to 25 MHz. A negatively dc biased discharge electrode (-2 kV), 25 μm thick, sits on top of the dielectric layer (19 μm thick and $\epsilon_r = 20$) and has a 35 μm opening, which exposes the underlying dielectric. A less negatively dc biased screen electrode, 40 μm thick, biased with -1950 V is separated from the discharge electrode by another dielectric (25 μm thick and $\epsilon_r = 20$) and acts as an anode switch to extract charges and narrow the current beam. The extracted electron current is accelerated toward a grounded electrode covered with a 25 μm dielectric sheet having ϵ_r up to 12.5. This dielectric-covered grounded electrode is separated from the screen electrode by a gap of 410 μm . The lateral spacings between the mDBD apertures are tens to hundreds of micrometers. The side boundaries in the simulation are grounded and placed far from the mDBD apertures using a

progressively coarser mesh so that the potential calculation will not be affected by the side boundaries. The top and bottom boundaries are also grounded, as in the actual device. All the dielectrics used in the model are perfect insulators—the conductivity is zero and the surface charges on the dielectrics are laterally immobile.

In this study, the mDBD is filled with N_2 at 1 atm with a small amount of O_2 serving as an impurity at room temperature, 300 K. This selection of gas mixture reflects that used in experiments. The ratio of N_2/O_2 varies from 99.99/0.01 to 90/10. A reduced reaction mechanism contains a subset of the reactions described in [28, 29] to limit the magnitude of calculation. The reduced reaction mechanism includes N_2 , $N_2(v)$, N_2^* , N_2^{**} , N_2^{***} , N_2^+ , N_4^+ , N , N^* , N^+ , O_2 , O_2^* , O_2^+ , O_2^- , O_3 , O^- , O , O^* , O^+ and electrons. The states N_2^* and N_2^{**} are nominally $N_2(A, B)$ and $N_2(C)$ although the latter is treated as a lumped state including transitions higher than $N_2(C)$, and N_2^{***} is nominally $N_2(a')$. The discharge is initiated by placing a plasma cloud of radius $100 \mu\text{m}$ centered in each mDBD cavity with a peak electron density of 10^{12}cm^{-3} . Many rf cycles are then computed until either quasi-steady-state conditions are achieved or long-term trends are discernable. Each aperture in an actual array is circular, which would require a three-dimensional model to resolve. Our model, being 2D, resolves side-by-side apertures as slots in a Cartesian geometry.

3. mDBD plasma properties

The plasma dynamics of a single-aperture mDBD in a similar geometry have been previously investigated [27], and so the fundamental properties of single mDBDs will be briefly discussed. The operating conditions are 1 atm $N_2/O_2 = 99.99/0.01$ at 300 K. This impurity reflects the actual purity of the gas used in experiments and provides an unambiguous source of photoionization. As shown in figure 1, the rf electrodes are biased with -2 kV dc plus 1.4 kV rf voltage at 25 MHz. The discharge and screen electrodes are biased with -2 kV and -1950 V , respectively. The grounded electrode is about $400 \mu\text{m}$ above the screen electrodes, and is covered by a dielectric sheet of thickness $25 \mu\text{m}$ with relative permittivity $\epsilon/\epsilon_0 = 12.5$. The complete computational domain extends 1.45 mm on either side of the center mDBD. The time evolution of single aperture electron density and electric potential during an rf period is shown in figure 2(a). The electron density, electric field and potential in the mDBD cavity are shown in figure 2(b) at $t = 13.5 \text{ ns}$ when the top electrode begins to extract the electron plume. The applied rf voltage is shown in figure 2(c). The cycle begins with -2 kV on the rf electrode at $t = 0 \text{ ns}$, which is the same as the voltage on the discharge electrode. However, due to the positive charge deposited on the bottom dielectric in previous rf cycles, electrons are attracted toward the dielectric and begin to neutralize the positive charge. By $t = 15 \text{ ns}$, the negative charge collected on the bottom dielectric is sufficiently large that the electric field vectors are reversed and an electron flux starts to escape from the mDBD cavity. The screen electrode with a potential 50 V higher than the discharge electrode acts as an anode switch to help extract and focus the electron current. The re-entrant electric potential

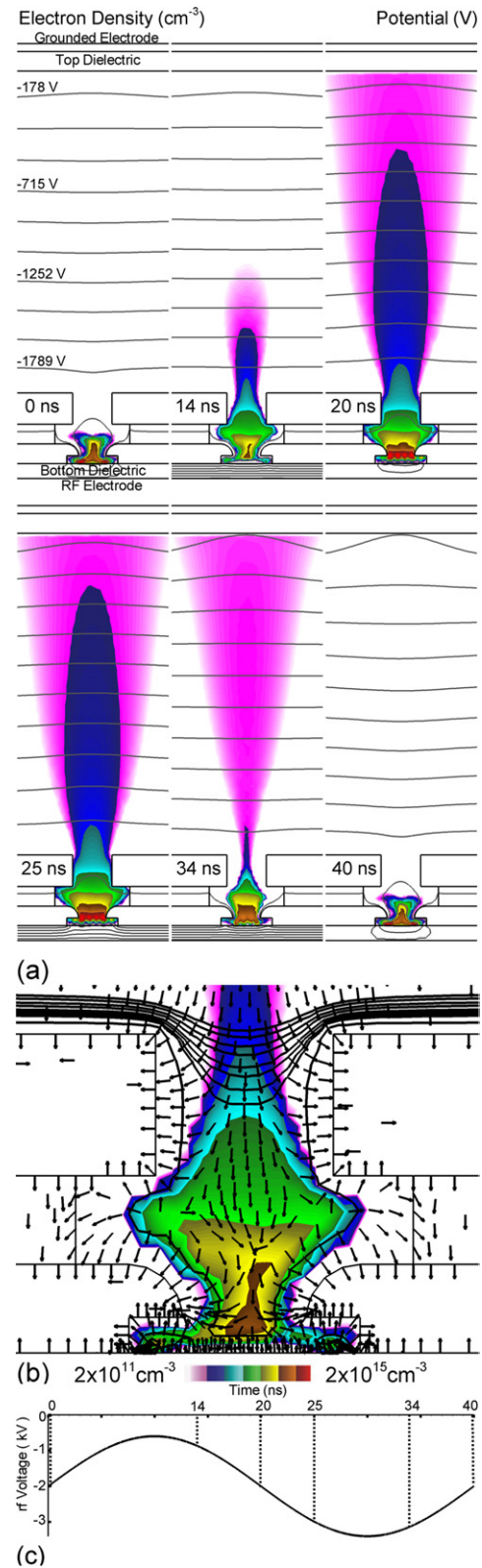


Figure 2. Electron current extraction produced by an rf voltage of 25 MHz. (a) Time evolution of electron density (color flood, cm^{-3}) and electric potential (contour lines, V) during a 40 ns rf period. The electron density is plotted on a log-scale over 4 decades (2×10^{11} – $2 \times 10^{15} \text{ cm}^{-3}$). (b) Electron density (color flood, cm^{-3}), electric field (vector, V cm^{-1}) and potential (contour lines, V) at $t = 13.5 \text{ ns}$ when electrons are extracted; (c) rf driving voltage. The instantaneous electric field vectors show only the orientation but not the magnitude of the field which help extract and focus the electron beam.

contours in the opening of the screen electrode, as shown in figure 2(b), aid in focusing the plume when extracting the electrons toward the top dielectrics.

As the rf voltage decreases to -2 kV at $t = 20$ ns, there is no net external rf field applied to the cavity while a large negative potential remains on the bottom dielectric due to the previously collected negative charges. The electron plume is then expelled out of the mDBD cavity toward the top dielectric-covered extraction electrode, which negatively charges the sheet. At the same time, the plasma is reignited in the cavity due to the avalanche of remaining residual electrons and secondary electron emission from the surface in the cavity produced by UV/VUV photons and ions. The current extraction is then enhanced as the rf voltage becomes slightly more negative at $t = 25$ ns. When the rf voltage becomes more positive (or less negative) at $t = 34$ ns, a sufficiently large amount of positive charge is collected on the bottom dielectric so that the negative charge is neutralized, the voltage drop is reduced and the electron plume begins to diminish. The cycle then repeats. The electron density in the mDBD cavity is of the order of $3 \times 10^{15} \text{ cm}^{-3}$, and is of order $5 \times 10^{11} \text{ cm}^{-3}$ adjacent to the top dielectric. As the electron current beam negatively charges the top dielectric, a negative surface potential is produced and electric potential lines are trapped into the dielectric target, as shown in figure 2(a) at $t = 40$ ns.

4. Small arrays of mDBDs

The plasma plumes extracted from the mDBD cavities interact with the top collection surface by successively charging the surface on a pulse-by-pulse basis. This charges the capacitance of the dielectric sheet which produces a negative surface potential, which results in additional lines of electrical potential in the dielectric. The acceleration produced by the resulting electric fields opposes the incoming plume of electrons. If the charging is spatially uniform, the collection of current from the electron plumes will uniformly decrease. If the charging of the surface is spatially non-uniform or the surface is in motion, the retarding electric fields may perturb the incidence plumes in a non-uniform or asymmetric manner.

To investigate these dynamics, an array of three mDBDs was simulated with a spacing of $300 \mu\text{m}$, as shown in figure 3. The dielectric constant of the top dielectric is $\varepsilon/\varepsilon_0 = 1.25$, purposely chosen to be small to accelerate the consequences of charging. The voltages on the three rf electrodes are in phase with a -2 kV dc bias and a 1.4 kV rf bias at 25 MHz (a period of 40 ns). The resulting electron density is shown at the peak of the electron extraction for the 1st, 3rd, 5th, 7th and 12th pulse. The electrons extracted from the mDBDs are incident onto the top dielectric target. For the initial portion of the first pulse, the potential lines in the gap are essentially uniform and parallel. The unperturbed electron plumes are accelerated vertically upward to the dielectric and begin to charge the surface, which traps the potential lines in the dielectric sheet. Meanwhile, these three electron plumes are below the space charge limit of affecting their neighbors and so are extracted independently. By 20 ns, there is enough

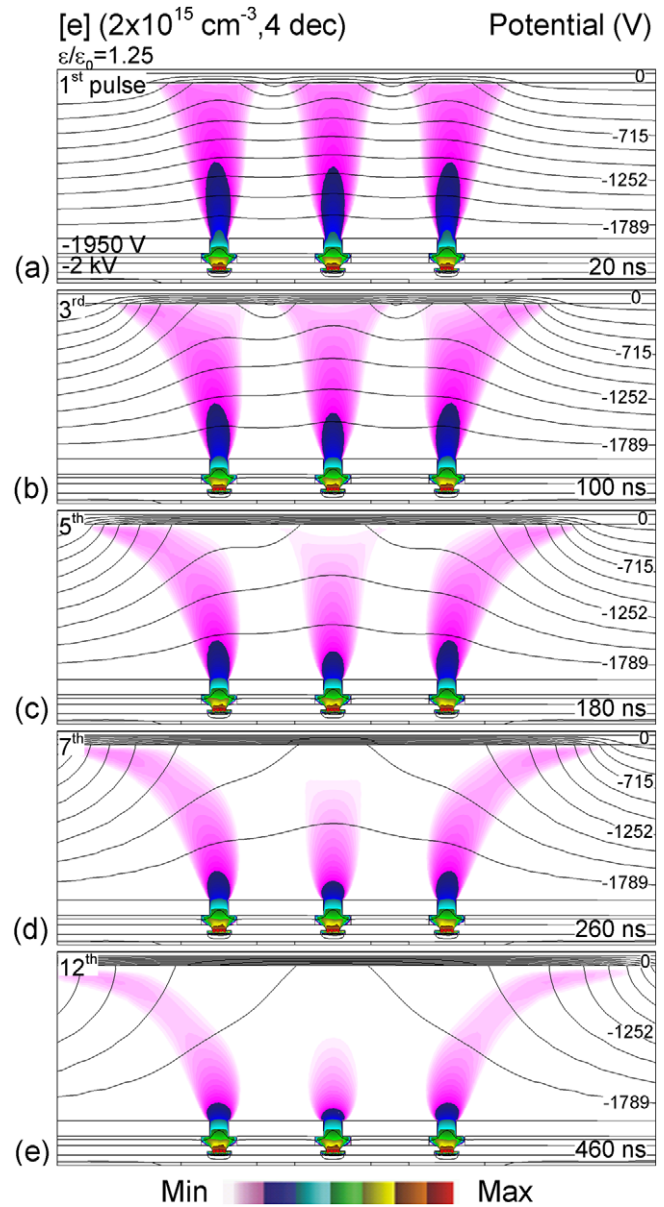


Figure 3. mDBD array with a spacing of $300 \mu\text{m}$ and target dielectric constant of $\varepsilon/\varepsilon_0 = 1.25$. Electron density (color flood, cm^{-3}) and electric potential (contour lines, V) at the peak of electron current extraction for the (a) 1st, (b) 3rd, (c) 5th, (d) 7th and (e) 12th rf pulse. The electron density is plotted on a log-scale over 4 decades (2×10^{11} – $2 \times 10^{15} \text{ cm}^{-3}$). The electron plume is largely warped toward the less charged dielectric by the 12th pulse.

charging of the dielectric in spots above the mDBD apertures so that horizontal components of the electric field are generated, which in turn begin to warp outward the two outside electron plumes. The center plume, seeing symmetric charging on either side, remains nearly vertical.

As the pulsing continues, negative charging of the dielectric target continues and the retarding potential increases. By the 3rd pulse (100 ns), the potential at the dielectric surface is as large as -1160 V, half of the initial extraction potential. The potential is non-uniform and varies by 300 V laterally across the surface. With an additional two pulses (180 ns), the negative charging and negative potential of the dielectric are

sufficiently large that the center electron plume is diminished in intensity and the rate of surface charging decreases. Electric fields with components parallel to the dielectric are produced by the charging and deflect the outer plumes in the direction of the largest electric field, which is now toward the uncharged dielectric on the boundary. By the 12th pulse (460 ns), the center plume is extinguished as the potential difference between the top dielectric and the focusing screen electrode is insufficient to extract additional charge. The outer plumes are deflected by more than the spacing between the mDBDs. This deflection in printing diminishes the quality of the latent image and poses a challenge to achieving a high-resolution image [18, 19].

Since the onset of the divergence of the current is inversely proportional to the charging time (or the capacitance) of the top dielectric, a larger capacitance of the top dielectric having a larger charging time should delay the divergence. This expectation is illustrated in figure 4 where electron plumes and electric potential contours are shown for the same conditions as figure 3 except for the top surface having a larger dielectric constant $\varepsilon/\varepsilon_0 = 12.5$. With the larger permittivity and capacitance of the top dielectric, obtaining a given surface potential requires more charge accumulation, and so divergence of the current begins later. The plumes from each of the three mDBDs maintain their vertical trajectories through the first 10 pulses, and only at $t = 460$ ns are the electron plumes beginning to become significantly warped.

Although the majority of ionization occurs in the mDBD cavity, some ionization does occur as the electron plume transits the gap. Due to low mobility of the positive ions (dominantly N_4^+ produced by three-body reactions of the originally produced N_2^+) and their slow drift toward the negatively biased screen electrode, ions tend to accumulate in the gap pulse to pulse. The total charge density and electric potential are shown in figure 5 for several rf pulses. A net positive charge density of $7.5 \times 10^{11} \text{ cm}^{-3}$ is initially produced after the first few rf cycles in the path of the electron plume. The more mobile electrons are accelerated out of the gap on a pulse-by-pulse basis leaving the positive ions that were produced in the gap. As the electron plumes are diverted by charging of the dielectric, electron impact ionization in the gap occurs in the deflected path and the accumulation of positive charge follows the trajectories of the plumes. The positive charge density that remains in the gap is insufficient to significantly perturb the potential lines, as the potential is dominantly determined by the dielectric charging. (For these conditions, the negative ion density in the gap is small, $8.5 \times 10^9 \text{ cm}^{-3}$.) However, the net positive charge density is large enough, $3.7 \times 10^{12} \text{ cm}^{-3}$, near the apertures in the screen electrodes to produce a small concavity of the potential contours. An auxiliary average electric field is produced to aid in current extraction and help focus the electron beam due to this additional concavity of the electric potential lines. The accumulated positive ion density near the apertures and the extracting electric field increase with successive discharge pulses. As a result, the peak electron density increases at early pulses before the surface charge on the top dielectric reduces the extracting field.

With the small impurity of O_2 in the current gas mixture $N_2/O_2 = 99.99/0.01$, the influence of negative ions is

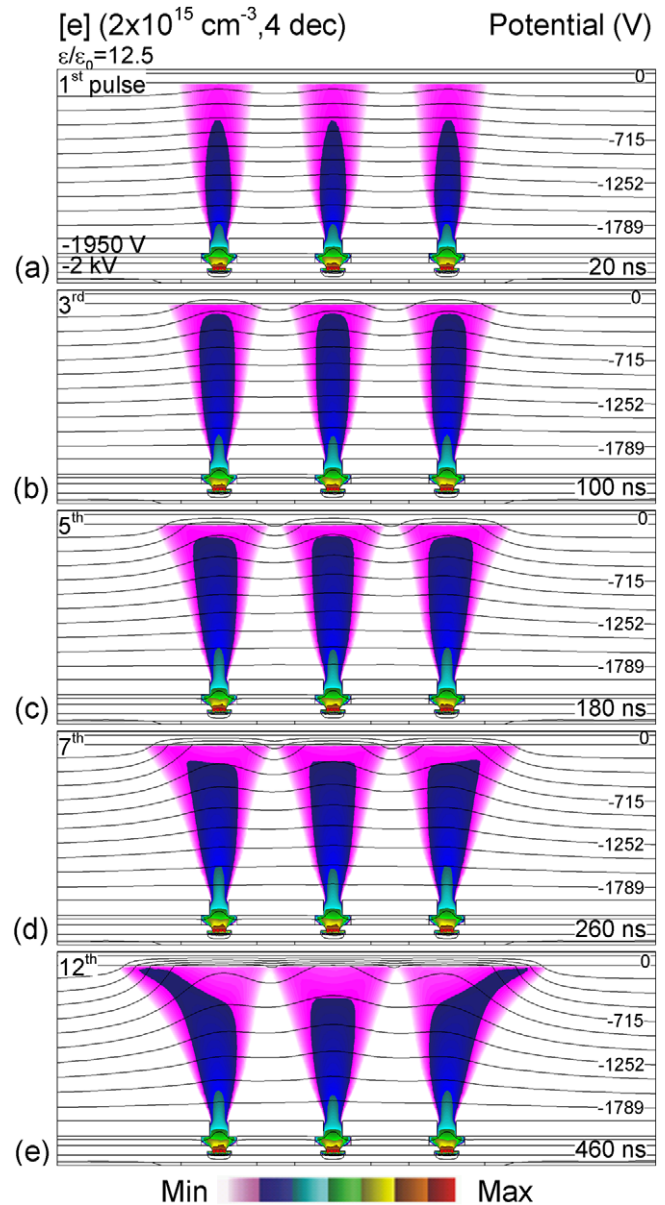


Figure 4. mDBD array with a spacing of $300 \mu\text{m}$ and larger target dielectric constant $\varepsilon/\varepsilon_0 = 12.5$. Electron density (color flood, cm^{-3}) and electric potential (contour lines, V) at the peak of electron current extraction for the (a) 1st, (b) 3rd, (c) 5th, (d) 7th and (e) 12th rf pulse. The electron density is plotted on a log-scale over 4 decades (2×10^{11} – $2 \times 10^{15} \text{ cm}^{-3}$). Divergence of the current begins later due to the longer charging time of the target dielectric.

inconsequential. With increasing O_2 content, however, electron attachment and negative ions begin to play more important roles. The total charge density, surface potential and time-integrated electron flux after 11 pulses (450 ns) for O_2 fractions of 0.01–10% are shown in figure 6. The net negative charge density (ρ^-) and the net positive charge density (ρ^+) shown in figure 6 are separated by a white contour line. Below 0.1% O_2 , positive ions (mainly N_4^+) accumulate close to the apertures and produce an average extracting electric field, while negative ions (mainly O^-) slowly drift to the top anode-like dielectric. The fractional electron loss due to attachment is small, and the mDBDs behave as though they are

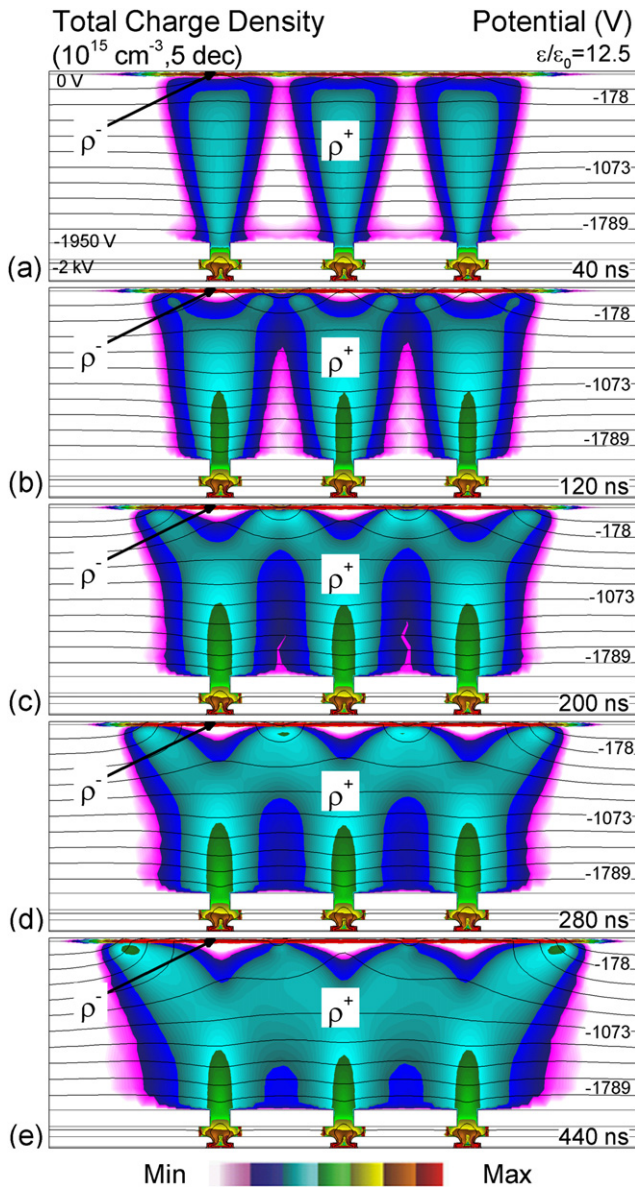


Figure 5. Total charge density (color flood, cm^{-3}) and electric potential (contour lines, V) for the (a) 1st, (b) 3rd, (c) 5th, (d) 7th and (e) 11th rf pulse. The charge density is plotted on a log-scale over 5 decades (10^{10} – 10^{15} cm^{-3}). Electrons in the plumes are accelerated toward the top dielectric and only heavy positive ions are left in the gap. An additional concavity in the potential is produced by the net positive charge in the gap, which helps in extracting and focusing the electron current beam before surface charging becomes dominant.

electro-positive plasmas. The concave electric potential lines close to the screen electrode help focus the electron beam.

When the gas mixture increases to 1% and 10% O_2 , electron attachment becomes a significant electron loss mechanism and more negative ions are then produced along the electron extraction path. The increasing negative ion density reduces the extracting electric field by reducing the net positive charge density. By an O_2 fraction of 10%, the net negative charge extends nearly to the opening in the screen electrode and the previously concave electric potential lines are reversed to be convex. The convex electric potential lines produced

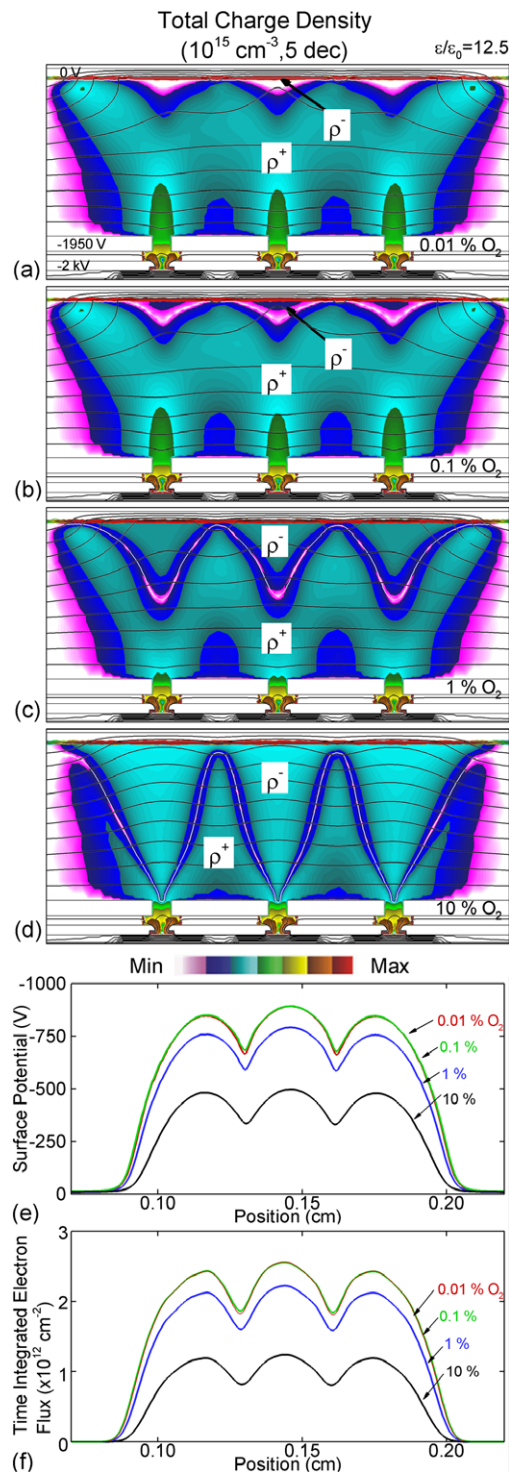


Figure 6. Net negative (ρ^-) and positive (ρ^+) total charge density (color flood, cm^{-3}) and electric potential (contour lines, V) in a gap filled with N_2/O_2 mixtures with O_2 contents of (a) 0.01%, (b) 0.1%, (c) 1% and (d) 10%. The charge density is plotted on a log-scale over 5 decades (10^{10} – 10^{15} cm^{-3}) after the 11th pulse. A white line separates regions of positive and negative charges. The resulting (e) top potential (V) on the top dielectric surface and (f) time-integrated electron flux (cm^{-2}) decrease with increasing O_2 content.

by net negative charges now defocus the extracted electron beam. The time-integrated electron flux on the top dielectric is then proportionately smaller and more uniform, as shown in figure 6(f). A consequence of the decrease in the integrated

electron current is a decrease in the surface potential on the dielectric. The surface potential on the top dielectric for O₂ fractions of 0.01–10% after 11 pulses is shown in figure 6(e). With an O₂ fraction <0.1%, the negative peak surface potential remains near –900 V. When the O₂ fraction increases to 10%, the surface potential drops to –500 V.

The O₂ impurity also provides a volumetric photoionization source (S_{ph}). By increasing the O₂ fraction from 0.01% to 10%, S_{ph} increases from 2.5×10^{17} to $8.2 \times 10^{19} \text{ cm}^{-3} \text{ s}^{-1}$, which is still small compared with electron impact ionization sources. Having said that, this small photoionization source is fairly uniform throughout the volume of the mDBD cavity, and so serves to seed electrons that eventually avalanche in locally large electric fields. In the same way, UV photons from long-lived excited states continuously seed secondary electrons by photoemission at the dielectric and electrode surfaces, which helps in facilitating the re-ignition of the plasma.

The uniformity and charging of the dielectric are functions of the mDBD spacing, and this can be used to advantage depending on the application. For example, if uniform charging over large areas is desired without modulation, more closely spaced mDBDs can be used. If truly independent charging of spots on the dielectric is desired, more widely spaced mDBDs can be used. For example, the electron density and electric potential for successive pulses are shown in figures 7(a)–(f) for a spacing between the mDBDs of 100 μm . The electron density and potential after the 12th pulse are shown in figure 7(g) for a spacing of 600 μm . The surface potentials after the 12th pulse (460 ns) for spacings between the mDBDs of 100, 300 and 600 μm are shown in figure 7(h). The repetition rate is 25 MHz (40 ns cycle). With the 100 μm spacing, the electron density in the plume adjacent to the top surface initially increases (first three pulses) prior to the negative charging of the surface beginning to dominate and deflecting the electron current. Decreasing the aperture spacing does not change the current extraction process. However, the three electron plumes do merge to form a single current beam as the interactions between the electron beams are not significant. Due to the merging of the plumes, the electron current is larger in amplitude and broadened in width, producing a less modulated and larger (more negative) surface potential. The peak surface potential reaches –1060 V on the 12th pulse due to the merged electron plumes. As the spacing is increased to 600 μm , the charging of the dielectric by the electron plumes becomes more independent and the individual electron plumes are not significantly perturbed by the charging produced by its neighbor. The peak surface potential produced by each individual mDBD plume drops to –750 V.

Since divergence of the current occurs within 100s of nanoseconds and is dependent on the capacitance (charging time) of the top dielectric and accumulation of ions in the gap, the charging process should be sensitive to the rf driving frequency. The electron density and electric potential after four rf cycles for frequencies of 2.5–25 MHz are shown in figure 8. As a point of reference, the peak electron density during each rf cycle is shown in figure 9(a) for site A adjacent to the target dielectric (see figure 1(b) for location). The

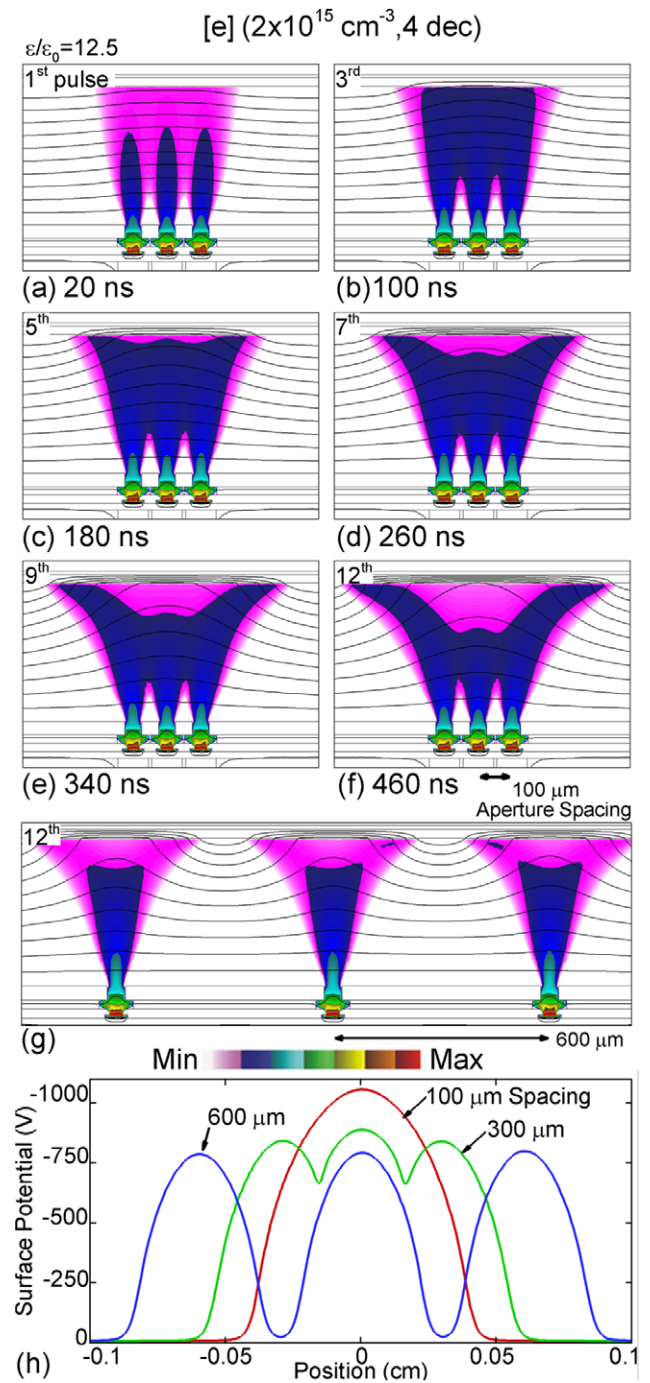


Figure 7. A more uniform current beam with a higher intensity can be achieved by reducing the mDBD spacing. Electron density (color flood, cm^{-3}) and electric potential (contour lines, V) for the (a) 1st, (b) 3rd, (c) 5th, (d) 7th, (e) 9th and (f) 12th rf pulse. The electron density is plotted on a log-scale over four decades (2×10^{11} – $2 \times 10^{15} \text{ cm}^{-3}$). (g) Electron density and potential after the 12th pulse for a 600 μm spacing. (h) Surface potential on the top dielectric after the 12th pulse for spacings of 100, 300 and 600 μm between the microdischarge cavities. A less modulated and higher peak potential results from merging of the closely spaced electron plumes.

electric potential on the surface of the top dielectric at the same time ($t = 500 \text{ ns}$) and the same pulse (4th) is shown in figures 9(b) and (c). Since the top dielectric is treated here as a perfect insulator, this potential profile reflects the charged

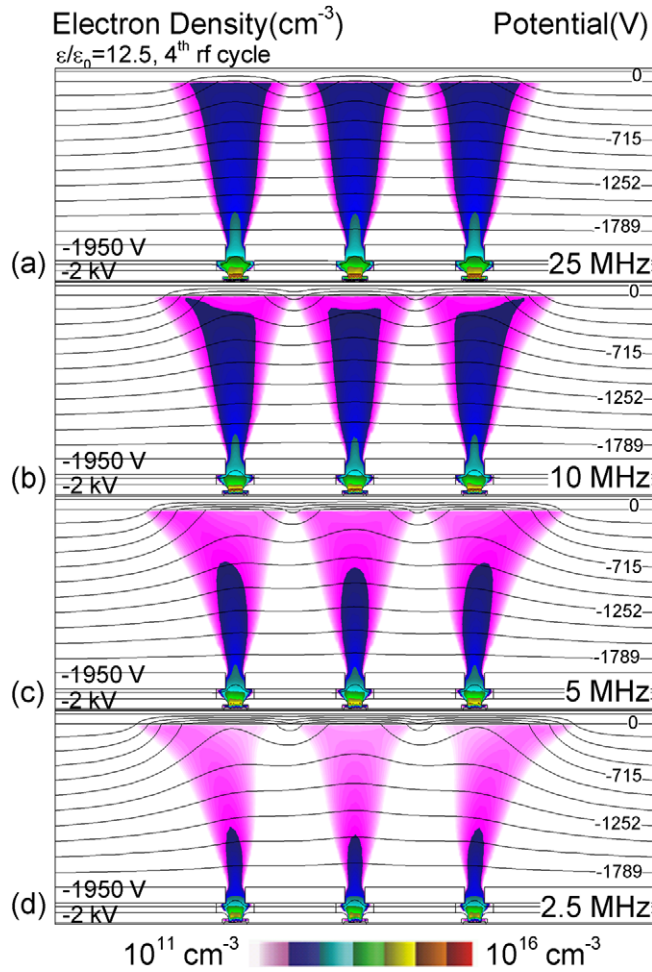


Figure 8. Electron density (color flood, cm $^{-3}$) and electric potential (contour lines, V) during peak current extraction on the 4th rf cycle for frequencies of (a) 25 MHz, (b) 10 MHz, (c) 6 MHz and (d) 2.5 MHz. The electron density is plotted on a log-scale over 5 decades (10^{11} – 10^{16} cm $^{-3}$). More negative voltage and charge density result on the top dielectric at a lower frequency due to the longer rf period.

particle fluence (cm $^{-2}$ —flux integrated over time) along the surface. In reality, it is likely that UV photon illumination of the top dielectric does provide some surface conductivity that might smear out the collected charge and hence the potential. At a high frequency, charge extraction is limited by the shorter rf cycle, while positive ions accumulating in the gap cannot respond to such a high frequency. These ions produce a positive space charge in the gap and help extract electrons out of the mDBD cavity. As a result, the peak electron density at site A initially increases due to this accumulation of positive ions, which produces a larger extraction field. The electron density then decreases with increasing number of pulses as a result of negative charging of the dielectric.

With lower frequencies and longer cycles, more electrons are extracted out of the mDBD cavity into the plume during early cycles. The plume then charges the dielectric, which retards the subsequent electron flux. Also, there is sufficient time for positive ions in the gap to drift downward to be collected by the screen and discharge electrodes, thereby reducing the accumulation of positive charge in the gap, which

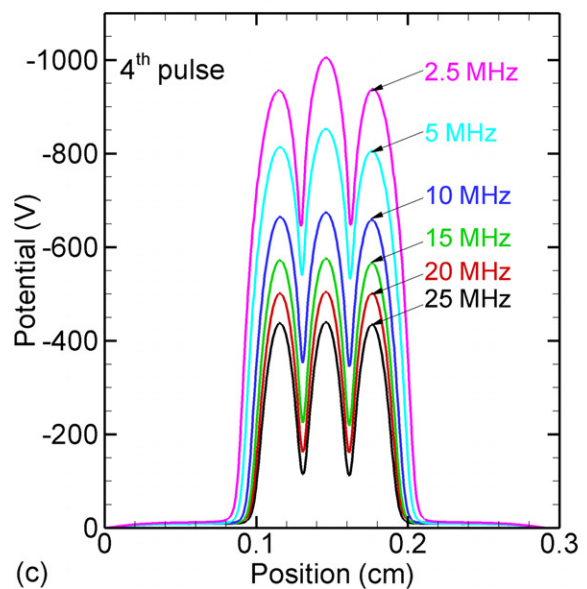
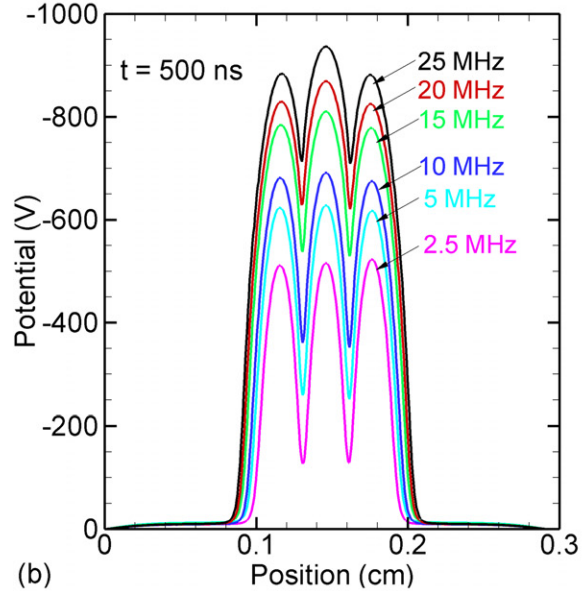
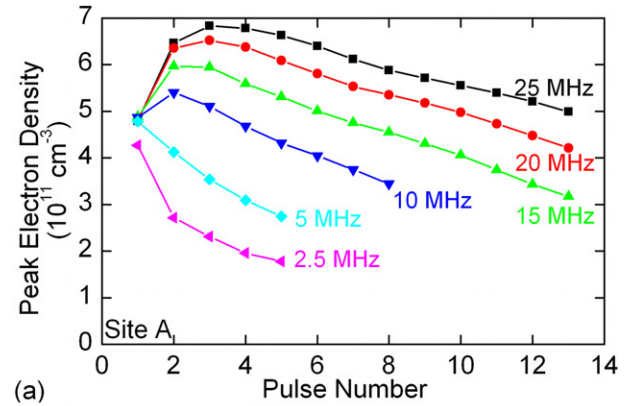


Figure 9. Plasma and charging characteristics for different rf frequencies. (a) Peak electron density (cm $^{-3}$) at site A (see figure 1) as a function of pulse number, (b) surface potential (V) at $t = 500$ ns and (c) surface potential after the 4th pulse. At higher frequencies, the peak electron density initially increases due to enhancements in the extracting field produced by positive ion accumulation. The electron density then decreases due to charging of the top dielectric. At lower frequencies, positive ions are collected by the screen electrode and the electron density decreases with increasing pulses.

would otherwise enhance electron extraction. Consequently, the peak electron density at site A decreases with increasing number of rf pulses. The charge collection on the top dielectric surface at a given time tends to be larger at higher frequencies. The electric potential on the top dielectric at $t = 500$ ns is more negative at a high frequency simply due to there being more charge collection as a result of the higher repetition rate. However, more charge is collected at a lower frequency for a given rf pulse. As a result, the surface potential is about half as negative at 25 MHz compared with 2.5 MHz. The larger current collection per pulse at a lower frequency is shown by the more negative potential after four pulses compared with a high frequency (-1000 V at 2.5 MHz compared with -400 V at 25 MHz). Although a non-uniform voltage can be generated by the surface charges on the top dielectric sheet, the resulting electric field parallel to the surface is typically not large enough to induce a surface discharge.

The ability to independently control the rf bias to each mDBD aperture provides the opportunity to tune the profile of the surface charging. This tuning capability is demonstrated by the electron density, electric potential and surface potential shown in figure 10 for an mDBD spacing of $300\ \mu\text{m}$. The electron density and potential are shown for the 1st, 3rd, 5th, 7th and 12th pulse. The applied voltage of the center rf electrode is delayed by two cycles (80 ns) compared with the outer electrodes that are excited in phase. The surface potential after 500 ns (12 pulses) for the center-delayed operation is compared with fully synchronized mDBDs in figure 10(f). The charging process of the center-delayed case is essentially the same as that of the in-synch case. However, with the center plume delayed by two pulses, there is proportionately less charge extracted from the mDBD and so less surface charging. With fully synched mDBDs, the surface potential is the largest (most negative) above the center mDBD, a result of the outer plumes being deflected and there being contributions to surface charging at the center by the adjacent plumes. By delaying the center mDBD, there is marginally less deflection of the outer plumes and less charging by the center plumes. The end result is that the peak surface potential above the center mDBD is reduced by 100 V (less negative), in this case becoming slightly less negative than the other peaks.

5. Concluding remarks

mDBD arrays are being developed for high-definition surface treatment and charging. Using results from a two-dimensional model, we investigated the plasma dynamics of a small array of mDBDs sustained in 1 atm N_2/O_2 mixtures, and the interaction between electron plumes through charging of the target dielectric. After electrons are produced in the mDBD cavities and extracted onto the target dielectric surface, a negative potential is generated, which deflects the incoming electron plumes. This divergence can be mitigated by increasing the dielectric constant (or charging time) of the target surface. Positive ions which accumulate in the gap also help extract charges by increasing the average extraction field. With increasing oxygen fraction, electron attachment processes begin to dominate. As a result, the electron flux

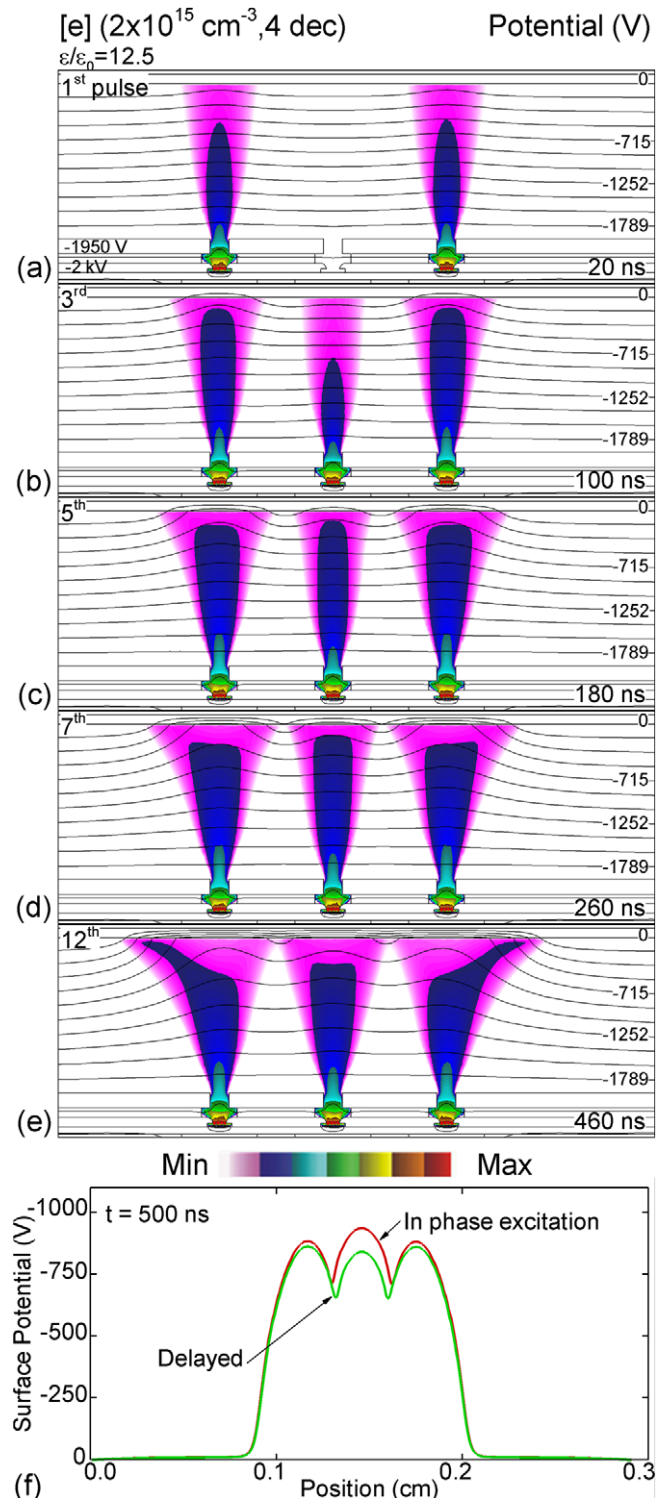


Figure 10. Independently controlled mDBDs demonstrated by delaying the rf voltage on the center microdischarge by 2 rf periods. Electron density (color flood, cm^{-3}) and electric potential (contour lines, V) for the (a) 1st, (b) 3rd, (c) 5th, (d) 7th and (e) 12th rf pulse. The electron density is plotted on a log-scale over 4 decades (2×10^{11} – 2×10^{15} cm^{-3}). (f) Surface potential on the top dielectric at $t = 500$ ns (12th pulse) for in-phase and center-delayed rf excitation. Tuning of the surface potential is enabled by controlling the onset of individual microdischarges, in this case a decrease in the potential of the center peak 100 V due to the two-period delay.

extracted from the mDBD cavity is additionally hindered by negative ion charge accumulation in the gap. Collection of charge on the top dielectric is then reduced with increasing oxygen content.

Uniformity of charging is a sensitive function of mDBD spacing. Reducing the mDBD spacing merges plumes and reduces modulation of the charging. Increasing the spacing between the mDBD reduces the deformation of the plumes by the charging produced by adjacent plumes. The surface potential profiles can be tuned by independently controlling the timing and number of pulses from the individual mDBD apertures. The plumes also indirectly interact with each other through the space charge they produce in the gap. This is, however, a cumulative effect. Due to the large extracting electric field and high mobility of electrons, the space charge provided by the electron density in the gap during a single pulse is not large enough to perturb the neighboring plume. However, the accumulation of low-mobility ionic charge (either positive or negative) during successive pulses can produce sufficient space charge to perturb neighboring plumes. In this sense, more closely spaced mDBDs will be more perturbing to their neighbors. In all cases, charging of the dielectric and its associated electric fields ultimately dominate in perturbing the plume.

Acknowledgments

This work was supported by HP Research Labs, the Department of Energy Office of Fusion Energy Science and the National Science Foundation.

References

- [1] Kogelschatz U 2003 *Plasma Chem. Plasma Process.* **23** 1
- [2] Kim H H 2004 *Plasma Process. Polym.* **1** 91
- [3] Eliasson B, Hirth M and Kogelschatz U 1987 *J. Phys. D: Appl. Phys.* **20** 1421
- [4] Borcia G, Anderson C A and Brown N M D 2003 *Plasma Sources Sci. Technol.* **12** 335
- [5] Sira M, Trunec D, Stahel P, Bursikova V, Navratil Z and Bursik J 2005 *J. Phys. D: Appl. Phys.* **38** 621
- [6] Fang Z, Xie X, Li J, Yang H, Qiu Y and Kuffel E 2009 *J. Phys. D: Appl. Phys.* **42** 085204
- [7] Lucas N, Hinze A, Klages C P and Büttingenbach S 2008 *J. Phys. D: Appl. Phys.* **41** 194012
- [8] Kong M G, Kroesen G, Morfill G, Nosenko T, Shimizu T, van Dijk J and Zimmermann J L 2009 *New J. Phys.* **11** 115012
- [9] Ayan H, Fridman G, Gutsol A F, Vasilets V N, Fridman A and Friedman G 2008 *IEEE. Trans. Plasma Sci.* **36** 504
- [10] Penache C, Gessner C, Betker T, Bartels V, Hollaender A and Klages C-P 2004 *IEE Proc. Nanobiotechnol.* **151** 139
- [11] Kreitz S, Penache C, Thomas M and Klages C-P 2005 *Surf. Coat. Technol.* **200** 676
- [12] Boeuf J P 2003 *J. Phys. D: Appl. Phys.* **36** R53
- [13] Becker K H, Schoenbach K H and Eden J G 2006 *J. Phys. D: Appl. Phys.* **39** R55
- [14] Park S J, Eden J G, Jain K and Klosner M A 2006 *Japan. J. Appl. Phys.* **45** 8221
- [15] Readle J D, Tobin K E, Kim K S, Yoon J K, Zheng J, Lee S K, Park S J and Eden J G 2009 *IEEE Trans. Plasma Sci.* **37** 1045
- [16] Fontanil M G L *et al* 1992 *US Patent* No 5,086,257
- [17] Cho K D, Tae H S and Chien S I 2003 *IEEE Trans. Electron Devices* **50** 359
- [18] Leoni N J, Gila O, Lee M H and Hanson E G 2010 *US Patent* No 7,764,296
- [19] Kubelik I 1995 *US Patent* No 5,450,103
- [20] Nie Q Y, Ren C S, Wang D Z, Li S Z, Zhang J L and Kong M G 2007 *Appl. Phys. Lett.* **90** 221504
- [21] Feng Y, Ren C S, Nie Q Y and Wang D Z 2010 *IEEE Trans. Plasma Sci.* **38** 1061
- [22] Tang D T, Ren C S, Wang D Z and Nie Q Y 2009 *Plasma Sci. Technol.* **11** 293
- [23] Shirafuji T, Kitagawa T, Wakai T and Tachibana K 2003 *Appl. Phys. Lett.* **83** 2309
- [24] Bedanov V M and Peeters F M 1994 *Phys. Rev. B* **49** 2667
- [25] Gurevich E L, Zanin A L, Moskalenko A S and Purwins H G 2003 *Phys. Rev. Lett.* **91** 154501
- [26] Xiong Z, Robert E, Sarron V, Pouvesle J-M and Kushner M J 2012 *J. Phys. D: Appl. Phys.* **45** 275201
- [27] Wang J-C, Leoni N, Birecki H, Gila O and Kushner M J 2013 Electron current extraction from rf excited micro-dielectric barrier discharges *J. Appl. Phys.* **113** 033301
- [28] Dorai R 2002 Modeling of atmospheric pressure plasma processing of gases and surfaces *PhD Thesis* University of Illinois (<http://uiigelz.eecs.umich.edu/theses.html>)
- [29] Akishev Y, Grushin M, Karalnik V, Petryakov A and Trushkin N 2010 *J. Phys. D: Appl. Phys.* **43** 215202